Synergistic effect of Ru-N_4 sites and Cu-N_3 sites in carbon nitride for highly selective photocatalytic reduction of CO_2 to methane

Lei Zeng,[a] Jiewei Chen,[b] Lixiang Zhong,[a] Wenlong Zhen,[a] Yee Yan Tay,[c] Shuzhou Li,[a] Yanggang Wang,*[b] Limin Huang,*[b] Can Xue*[a]

[a] School of Materials Science and Engineering, Nanyang Technological University, 50 Nanyang Avenue, 639798, Singapore

[b] Department of Chemistry, Southern University of Science and Technology, 1088 Xueyuan Avenue, Shenzhen 518055, P. R. China

[c] Facility for Advanced Characterization, Testing & Simulation, Nanyang Technological University, 50 Nanyang Avenue, 639798, Singapore

---

* Corresponding author: School of Materials Science and Engineering, Nanyang Technological University, 50 Nanyang Avenue, 639798, Singapore. cxue@ntu.edu.sg (C. Xue), Department of Chemistry, Southern University of Science and Technology, 1088 Xueyuan Avenue, Shenzhen 518055, P. R. China. wangyg@sustech.edu.cn (Y.G. Wang), huanglm@sustech.edu.cn (L. M. Huang)

Abstract: Developing single-atom photocatalyst for selective conversion of CO_2 to valuable fuel is of great attraction but remains challenging. In this work, ruthenium and copper single atoms are for the first time simultaneously incorporated into polymeric carbon nitride (PCN) through a simple preassembly-coprecipitation-pyrolysis process. The obtained PCN-RuCu sample exhibited much higher selectivity (95%) for CH_4 production than the individual Ru or Cu decorated PCN during photocatalytic CO_2 reduction under visible-light irradiation. The atomically dispersed Ru-N_4 and Cu-N_3 moieties were confirmed by spherical aberration-corrected electron microscopy and extended X-ray absorption fine structure spectroscopy. Density function theory (DFT) calculations revealed that the co-existence of Ru-N_4 sites and Cu-N_3 sites can effectively tune the electronic structure of PCN, making the Ru sites account for photogenerated electron-hole pairs and the Cu sites for CO_2 hydrogenation. Moreover, the synergetic effect between Ru and Cu single atoms significantly promotes the consecutive hydrogenation processes of *CO species towards CH_4 production. Our studies provide a new understanding of the mechanism for photocatalytic reduction of CO_2 to CH_4, and pave a new way to design photocatalysts for the selective production of solar fuels.

Keywords: Dual-metal-atom, CO_2 photoreduction, methane production, selectivity

1. Introduction

Methane, an important fuel and chemical feedstock, has been widely applied in the industrial and civil fields. However, the combustion product, CO_2, which leads to global warming is vital to develop the circular carbon economy. Photocatalytic reduction of CO_2 to CH_4 is a feasible approach to become carbon neutral.[1-4] In this regard, many photocatalysts have been reported to realize the high conversion of CO_2 to fuels.[5-7] Polymeric carbon nitride (PCN) is the best metal-free semiconductor to trigger the photocatalytic CO_2 reduction so far, because of its visible light response and excellent reduction potential of photoelectrons in the conduction band[8, 9]. However, PCN still suffers from low selectivity for production mainly because of the complicated process of CO_2 reduction and charge carrier recombination.[10, 11] Deposition of a cocatalyst on PCN is an acclaimed method to provide active sites for CO_2 reduction and promote charge transfer. Many metals, especially noble metal nanoparticles, have proven as reliable cocatalysts for improving the photocatalytic activity of PCN. Nonetheless, the rarity and high cost of noble metals inevitably impede their development. Downsizing noble metals to clusters or even single atoms to maximize atom efficiency and using alternative low-cost metals are two workable strategies to address this issue. As we know, it is necessary to provide appropriate host materials to anchor and stabilize single-atom catalysts. PCN is an ideal support for loading and stabilizing single atoms, because the nitrogen atoms with lone-pair electrons in the cavities of PCN matrix can serve as anchoring sites.[12-15]

Single-atom decorated carbon nitride has already been reported to catalyze various chemical reactions,[16-19] for instance, Au single atom decorated carbon nitride for photocatalytic hydrogen evolution,[20] Mn/PCN for production of hydroxyl radicals in an acidic solution,[21] Pt-Ru/PCN for catalytic CO oxidation,[22] Co/PCN for photocatalytic overall water splitting,[23] Cu/PCN for functionalization of methane into ethanol,[24] and Fe/PCN for photocatalytic sulfonation of alkenes.[25] Lately, using PCN confined single atoms to achieve selective artificial photocatalytic CO_2 reduction is quite attractive. Chen et al. designed single-atom La-N charge-transfer bridges on PCN for highly efficient and selective photocatalytic conversion of CO_2 to CO.[26] Ji et al. synthesized a rare-earth Erbium single atom supported PCN that showed outstanding photocatalytic CO2RR performance.[27] Li et al. developed crystalline carbon nitride-supported copper single atoms to achieve nearly 100% CO selective from CO_2 photoreduction.[28] Wang et al. also reported single atom copper modified PCN for selective CO_2 photoreduction.[29] Many excellent photocatalysts have been reported for highly selective photocatalytic CO_2 reduction to CH_4.[30] However, the combination of single atom and PCN employed for photocatalytic conversion of CO_2 to CH_4 is rarely reported. As a matter of fact, the photocatalytic CO_2 reduction to CH_4 involves a series of complicated proton-coupled electron transfer steps. Hence, it is still challenging to use monometallic single atom cocatalyst decorated PCN photocatalyst for selective CH_4 production. As mentioned, a copper single atom is widely confirmed to activate CO_2 molecule.[31-34] Naturally, it is rational to introduce another metal single atom to boost the protonation process to achieve selective production of CH_4.

Herein, we simultaneously incorporate Cu and Ru single atoms into the PCN framework by using a preassembly-coprecipitation-pyrolysis method. The as-prepared PCN-RuCu sample presented 95% selectivity for methane production during visible-light-driven CO_2 reduction. The CH_4 production rate of PCN-RuCu was 8.1 and 51 times higher than that of individual Cu single atom decorated PCN (PCN-Cu) and PCN-Ru, respectively. The identified Cu-N_3 site and Ru-N_4 site are confirmed as active centers. The co-existence of Cu and Ru single atoms significantly affects the electron structure of PCN. The dσ orbital of Ru atom contributes to the composition of the highest occupied molecular orbital (HOMO) of PCN-RuCu. Under illumination, Ru atom accounts for photogenerated electron-hole pairs. Besides, when the intermediate species *CO adsorbs on the Ru site, the transformation of *CO to *CHO becomes much more favorable in thermodynamics. The synergetic effect between Ru and Cu single atoms greatly improves the consecutive hydrogenation process towards CH_4 production. This work presents an intriguing viewpoint to CO_2 photoreduction when depositing single atoms of two different metals in the PCN framework. Also, it provides us with a new strategy to design photocatalysts for the selective production of solar fuels.

2.Experimental Section

2.1 Materials. Melamine, copper nitrate hydrate ($Cu(NO_3)_2·3H_2O$), ruthenium(Ⅲ) chloride ($RuCl_3$, Ru content 45-55%), cyanuric acid, dimethyl sulfoxide (DMSO), triethanolamine (TEOA), sodium bicarbonate ($NaHCO_3$), and sodium borohydride ($NaBH_4$) were purchased from Sigma-Aldrich. All chemicals were used directly without further purification.

2.2 Synthesis of PCN-RuCu. The heterogenous ruthenium-copper dual atoms anchored in PCN was synthesized as follow: the desired $RuCl_3$ and $Cu(NO_3)_2·3H_2O$ as Ru and Cu precursors were dissolved in 10 mL DMSO at 120 °C for 30 min together with 0.50 g melamine, the obtained black solution was marked as solution A. 0.51 g cyanuric acid was added into 10 mL DMSO through ultrasonic for 30 min, the obtained transparent solution was marked as solution B. Then, solution B was slowly added into solution A, and the white precipitate was subsequently generated. The mixture was kept at 120 °C and stirred until 10 mL DMSO remained. The white powder precursor was obtained by filtration. The precursor was dried at 60 °C overnight after being washed with 150 mL deionized water and 100 mL ethanol. Finally, the powdered precursor was pyrolyzed at 550 °C under Ar atmosphere for 4 h in a tube furnace with a ramp rate of 2.3

°C min^{-1}. The resulted sample was denoted as PCN-RuCu. The sample PCN-Ru and PCN-Cu was prepared by following the same procedure with only one metal precursor. PCN-0 was prepared without any metal precursors.

2.3 Photocatalytic CO_2 Reduction. The CO_2 photoreduction reaction was performed in a 34 mL vial. 10 mg photocatalyst (PCN-0, PCN-Ru, PCN-Cu, or PCN-RuCu), 9 mL $NaHCO_3$ solution (3M) and 1 mL TEOA were added. The reactor was sealed and purged by purified CO_2 (99.99%) for 30 min, then reacted under a 300 W Xe lamp (Max-302, Asahi Spectra Co. Ltd.). The gas composition from the upper space above the liquid was analyzed by a GC (Shimadzu 2010) equipped with FID and TCD detectors every two hours. The liquid product was analyzed by a GC-MS (Agilent 5977B GC/MSD) at the end of reaction.

The CH_4 selectivity was calculated by equation (1):

$$CH_4 \text{ selectivity } (\%) = \frac{n_{CH_4}}{\left(n_{CO}+n_{CH_4}+n_{H_2}\right)} \times 100\% \quad (1)$$

2.4 Computational Details of DFT Analysis. Spin-polarized density functional theory (DFT) calculations were performed by using the Vienna ab initio simulation package (VASP).[35, 36] The ion-electron interactions were treated with the projected augmented wave (PAW) pseudopotentials, and the cut-off energy for plane-wave expansion was set at 400 eV. The general gradient approximation (GGA) parameterized by Perdew, Burke, and Ernzerhof (PBE) was used to model the electronic exchange-correlation energy.[37] All structures were fully relaxed by a conjugate gradient method until the force component on each atom was less than 0.02 eV/Å, and the convergence criterion of total energy in the self-consistent field method was set at 10^{-6} eV. The lattice constant of 2D g-C_3N_4 unit cell was optimized to be 6.809 Å. The thickness of vacuum was 20 Å, which is large enough to eliminate superficial interaction between different layers. A super cell composed of 2×2 g-C_3N_4 unit cells was adopted to host Cu (and Ru) atoms, and the k-point grid used for the Brillouin-zone integration was 3×3×1 sampled by the Monkhorst-Pack scheme.[38] A larger cell or more k-points yielded the same results in the test calculations.

The schematic diagrams of HOMO are obtained by CP2K package.[39] The wave functions were expanded in optimized double-ζ Gaussian basis sets (DZVP), and the plane waves were expanded with a cutoff energy of 400 Ry.

The Gibbs free energies (ΔG) of reaction intermediates were calculated to characterize the CO_2RR performance on g-C_3N_4 supported atoms. Adsorption energies of the CO_2RR intermediates were calculated by:

$\Delta E_{adsorbate} = E_{total} - E_{substrate} - E_{adsorbate}$,

where E_{total} and $E_{substrate}$ are the DFT energies of the system with and without adsorbate, respectively, and $E_{adsorbate}$ is calculated relative to CO_2, H_2O and H_2. The corresponding adsorption free energies of reaction intermediates were further corrected by zero-point vibrational energy E_{ZPE}, entropy TS, and solvation energy E_{sol} as follows:

$\Delta G_{absorbate} = \Delta E_{adsorbate} + \Delta\ (E_{ZPE} - TS + E_{sol})$,

where $\Delta G_{absorbate}$ was used to construct the free energy profiles. The solvation effects were simulated by using the Poisson-Boltzmann continuum-solvation model in the VASPsol code.[40] The temperature (T) was set at 298.15 K

2.5 Characterization. Powder X-ray diffraction patterns (XRD) were recorded with a Panalytical XRD, using Cu Kα radiation (λ=1.540598 Å) operated at 40 kV and 30 mA. SEM images were obtained by using a FESEM 6340F scanning electron microscope with accelerating voltage at 5.0 kV. The transmission electron microscopy (TEM) and high-resolution TEM images were recorded on a JEOL-2100F FETEM with an accelerating voltage of 200 kV. The aberration-corrected high angle annular dark field scanning transmission electron microscopy (HAADF-STEM) images were obtained by using a JEM-ARM200F operated at 80 kV. X-ray photoelectron spectroscopy (XPS) measurements were conducted on a Kratos AXIS Supra system. The C 1s peak at 284.8 eV was used as the reference to calibrate the XPS spectra. The specific surface area was calculated from N_2 adsorption-desorption isotherms measured by a surface area and porosity analyzer (Micromeritics, VacPrep 061/ Tristar Ⅱ) and using the Brunauer-Emmett-Teller (BET) equation. UV-Vis diffuse reflectance spectra (DRS) were measure by a Lambda 750 UV/Vis/NIR spectrophotometer (Perkin-Elmer, USA). Photoluminescence (PL) spectra were measured in the solid state with an Agilent Fluorescence Spectrophotometer (Cary Eclipse). The time resolved PL decay spectrum was detected by a fluorescence spectrometer (F950) with an excitation wavelength of 365 nm and the collected excitation wavelength was 500 nm. X-ray absorption near-edge structure (XANES) and extended X-ray absorption fine structure (EXAFS) analyses were conducted at the 1W2B beamline of the Beijing Synchrotron Radiation Facility. The electrochemical impedance spectroscopy (EIS) and transient photocurrent response were measured on electrochemical station (CHI660B, Shanghai Chenhua). The conventional three-electrode system was used to measure the electrochemical performance in 0.5M Na_2SO_4 solution. In detail, the working electrode was prepared by dropping 10 μL aqueous slurry comprised of 5 mg catalyst sample and 1 mL absolute ethanol containing 100 μL 0.05 wt.% Nafion solution. The counter electrode and reference electrode were Pt wire and Ag/AgCl electrode, respectively. The EIS was conducted at the frequency range from 0.01 Hz to 106 Hz with an AC voltage amplitude of 5 mV. For transient photocurrent response measurement, the light source was a 300 W Xe lamp with a cutoff filter (λ>420 nm).

3. Results and discussion

3.1 Structure analysis of photocatalysts.

The ruthenium and copper single atoms decorated polymeric carbon nitride (PCN-RuCu) was prepared through a preassembly-coprecipitation-pyrolysis method, shown in Figure 1(See supporting information for details). Briefly, melamine, $RuCl_3$, and $Cu(NO_3)_2$ were dissolved and mixed in dimethyl sulfoxide (DMSO), followed by precipitation upon adding cyanuric acid. The precipitate was separated and calcined under Argon atmosphere at 550 °C for four hours. In this condition, polymeric carbon nitride could be formed through condensation of preassembled structure from melamine and cyanuric acid with Ru and Cu atoms concomitantly immobilized in the PCN framework. The pure PCN sample was also synthesized under the same condition without using any metal precursors (denoted as PCN-0). For comparison, control samples were obtained through the same preassembly-coprecipitation-pyrolysis methods using either $RuCl_3$ or $Cu(NO_3)_2$, denoted as PCN-Ru and PCN-Cu, respectively.

In the X-ray diffraction (XRD) spectra (Figure S1), all samples exhibited a similar XRD pattern with typical graphitic carbon nitride,[41, 42] and showed no peaks related to the metals or compounds of ruthenium and copper. Transmission electron microscopy (TEM) and scanning electron microscopy (SEM) images (Figure 2A & Figure S2) revealed that all prepared PCN samples featured hollow sphere structures, suggesting that the morphology was not affected by the incorporation of metal precursors. We did not observe any nanoparticles of metals or metal compounds in the high-resolution TEM image of PCN-RuCu (Figure 2B). Moreover, by using aberration-corrected high-angle annular dark-field scanning transmission electron microscopy (HAADF-STEM) (Figure 2C), we could identify metal single atoms as bright spots (highlighted by red circles) on the edge of PCN and the corresponding distribution of the individual ruthenium atoms and copper atoms coexisted on the PCN-RuCu sample. Notably, the bright spots were separate, and no aggregates could be found in HAADF-STEM images. Meanwhile, there was no conspicuous overlap of elemental signal between Ru and Cu in the EDS mapping image. It suggested that the distribution of Ru single atom and Cu single atom was discrete and no Ru-Cu dimers were formed. Besides, the content of Cu and Ru in the PCN-RuCu sample was measured by inductively coupled plasma-mass spectroscopy (ICP-MS) showing the mass percentage of elemental Cu and Ru in PCN-RuCu as 2.44% and 0.60%, respectively. In comparison, the PCN-Cu sample contained 2.57% Cu atoms that were also uniformly dispersed in the PCN framework (Figure S3). Interestingly, the PCN-Ru sample, having 0.56% elemental Ru, presented both individual Ru atoms and small Ru clusters (Figure S4). This observation suggested that the free Ru atoms, which were created during thermal calcination, may be inclined to diffuse on the PCN surface and agglomerate into clusters. Nevertheless, when Cu atoms co-exist and distribute in the PCN framework, the diffusion of Ru atoms might be restricted by the nearby Cu atoms, preventing the formation of Ru clusters in the PCN-RuCu sample.

The chemical states of metal species on PCN-RuCu were analyzed by X-ray photoelectron spectroscopy (XPS). As shown in Figure 3a, the Ru 3p XPS peaks of PCN-RuCu, at 462.2 eV for Ru 3p3/2 and 484.4 eV Ru 3p1/2, show no shift as compared to that of PCN-Ru. Similarly, in figure 3b, the Cu 2p XPS peaks in PCN-Cu and PCN-RuCu emerge at the same position at 932.4 eV for Cu 2p3/2 and 952.1 eV for Cu 2p1/2, which can be assigned to Cu(Ⅰ).[43, 44] It suggests no direct interaction or bonding between the Ru atom and Cu atom in the PCN-RuCu sample. To determine the valence state of Ru in the sample, we employed NaBH4 to treat the PCN-Ru sample to convert all Ru species to Ru(0) nanoparticles on PCN, and obtained a control sample, PCN-Ru-$NaBH_4$, which shows Ru 3p XPS peaks at 462.0 eV and 484.0 eV (Figure S5). Besides, the Ru 3p XPS peak of $RuCl_3$, at 464.3 eV and 486.5 eV, was also measured in Figure S5. Thus, we believe that the valence of Ru in PCN-Ru and PCN-RuCu should be between 0 and +3. The slight shift of Ru 3p peaks between PCN-Ru and PCN-Ru-$NaBH_4$ suggests that the individual Ru atoms in PCN-Ru have more intense binding with the nearby N atoms than the Ru nanoparticles in PCN-Ru-$NaBH_4$. In short, the XPS results indicate that in PCN-RuCu, the two metal elements, Cu and Ru, are distributed on the PCN surface as single atoms of Cu(I) and Ru(n) ($0<n<3$) without direct interaction between them. In figure 3d, the Ru K-edge XANES over PCN-Ru and PCN-RuCu display similar intensity. It is higher than that of Ru foil but lower than that of RuO_2, suggesting the oxidation state of Ru^{n+} ($0<n<4$) in PCN-Ru and PCN-RuCu is the same.[22] Compared with Cu foil and CuPc, the XANES of PCN-Cu shows a curve similar to that of CuPc reference, identifying the oxidized $Cu^{\alpha+}$ ($0<\alpha<2$). Fourier transformed EXAFS spectra for PCN-Ru and PCN-RuCu show characteristic peaks at around 1.47 Å and 1.55 Å, respectively (Figure 3f). And it is close to Ru-O bond at 1.51 Å in RuO_2 reference. The reason for this phenomenon may be ascribed to the indistinguishable coordination bond between C, N, and O elements and Ru atoms.[45] Meanwhile, it can be determined that the Ru-Ru bond does not exist in PCN-Ru and PCN-RuCu, because the characteristic peak at 2.37 Å in the EXAFS of Ru foil can be assigned to Ru-Ru bond. This result is also further proven by the wavelet transform (WT). As shown in Figure 3c, different from the intensity maximum at ≈5.4-8.9 $Å^{-1}$ that arises from the Ru-O bond in RuO_2 and Ru-Ru bond in Ru foil, only one intensity maximum at about 4.7 $Å^{-1}$ is detected in PCN-Ru and in PCN-RuCu, which can be assigned to Ru-N bond. Besides, it also suggests that the incorporation of Cu single atoms does not change the coordination environment of Ru atoms, while the formation of Ru-Cu bond is not found as well.[46] In Figure

S5, the WT plots in PCN-RuCu show the maximum peak at 4.6 Å^{-1}, corresponding to the Cu-N coordination by contrasting with Cu foil and CuPc. In addition, no intensity maximum at 7.7 Å^{-1} corresponding to Cu-Cu coordination can be observed. It further illustrates the isolated feature of Cu species in PCN-RuCu. EXAFS curve fitting is carried out to acquire quantitative structural parameters of Ru sites and Cu sites in PCN-RuCu. Table S2 exhibits the EXAFS fitting parameters and the fitting curve is shown in Figure 3h. The coordination number of center Ru atoms is about 4.2 and the average bond length is 2.05 Å, suggesting that Ru atoms in PCN-RuCu are coordinated with four N atoms. Similarly, the fitting curve of Cu EXAFS is shown in Figure 3i, and the coordination number of Cu atoms is 3.1 and the average bond length is 1.94 Å, suggesting that Cu atoms in PCN-RuCu are coordinated with three N atoms.[47, 48]

3.2 Photocatalytic CO_2 reduction performance.

The photocatalytic activities of all samples for CO_2 reduction are compared in Figure 4. The gaseous products contained CO, CH_4, and H_2 for all samples. There were no liquid products such as methanol, formaldehyde, and formic acid, as confirmed by ^{1}H-NMR (Figure S6). After 8-hour visible-light irradiation, The PCN-RuCu sample, having single-atom catalysts of Cu and Ru, showed production of 1.54 µmol CH_4, 0.02 µmol CO, and 0.06 µmol H_2, giving the selectivity of methane as 95.1% (CH_4 selectivity = moles of CH_4/moles of all gas products) The carbon isotopic tracing was employed under the same photocatalytic reaction condition (Figure 4B) to confirm that the products, CO and CH_4, originate from the photocatalytic reduction of CO_2. Even after 5 cycles of repeated tests, the PCN-RuCu sample still maintained excellent CH_4 selectivity (~95%). The examination by HAADF-STEM (Figure S7) and XPS (Figure S8) showed no structural change on the PCN-RuCu sample after the photocatalytic tests.

In comparison, the PCN-0 sample without any cocatalyst showed a very low yield of gas products (0.01 μmol O, 0.19 μmol CH_4, and 0.09 μmol H_2) with CH_4 selectivity of only 65.5%. For the PCN-Ru sample, the major product was H_2 (10.13 μmol) with only 0.03 μmol CH_4 and 0.10 μmol CO. The high yield of H_2 might be attributed to the existence of Ru clusters in PCN-Ru. In contrast, Cu atoms are not an effective catalyst for HER, and thus the PCN-Cu sample presented a production of only 0.09 μmol H_2 with concomitant evolution of 0.59 μmol CH_4 and 0.03 μmol CO (CH_4 selectivity of 83.1%). It is worth noting that the PCN-RuCu sample here is chosen as the optimum mass ratio of Ru/Cu (1:5). The photocatalytic activity of PCN-RuCu sample with different ratios of Ru/Cu was shown in Figure S9. In addition, the CH_4 production in the present study was also compared with those from previous reports to prove the excellent photocatalytic activity of PCN-RuCu in Table S3.

3.3 Charge transfer efficiency and band structure.

It is clear to find that the simultaneous incorporation of Ru single atom and Cu single atom has greatly improved the selectivity towards CH_4 production in CO_2 photoreduction. To reveal the reason for high selectivity, the basic characteristics of photocatalyst involving charge transfer efficiency, optical property, and band structure were measured. In Figure 5a, dramatic PL quenching occurs after incorporation of single atoms relative to PCN-0, implying that intrinsic radiative recombination of photogenerated electron-hole pairs in single atom decorated PCN, especially in PCN-Cu and PCN-RuCu, has been substantially inhibited. Moreover, the time-resolved transient PL decay spectra were also measured (Figure 5b) and the results were fitted by a triexponential decay function (Table S3). The average lifetime of PCN-0, PCN-Ru, PCN-Cu, and PCN-RuCu is 6.78 ns, 5.42 ns, 1.54 ns and 1.56 ns, respectively. It is noteworthy that the average lifetime sharply decreases after incorporation of Cu single atoms, implying the electron transfer from PCN to Cu atoms is more effective, compared with Ru atoms.[49-51] The improved charge transfer dynamics is also confirmed by the transient photocurrent measurement (Figure 5c) and electrochemical impedance spectroscopy (EIS, Figure 5d). The optical properties and band structure of all samples were determined by ultraviolet-visible diffuse reflectance spectra (UV-vis DRS), valence XPS and UV photoelectron spectroscopy (UPS). As shown in Figure 5e, PCN-RuCu showed excellent visible light-harvesting ability. According to the Kubelka-Munk function, the intrinsic bandgaps of PCN-0, PCN-Cu, PCN-Ru and PCN-RuCu were calculated to be 2.69, 2.64, 2.71 and 2.56 eV, respectively (Fig. 5f).[52] As revealed by the VB XPS spectra (Fig. 5g), the VB maximum increased obviously after the incorporation of single atoms. Knowing the calculated bandgap values and measured VB energy (versus Normal hydrogen electrode, NHE) of PCN-0 (Figure S10), the band structure of these samples could be outlined[53] and compared in Figure 5h. Although the positions of the conduction band of single atom decorated PCN samples all shifted down in comparison with PCN-0, it still satisfied the potential of CO_2 reduction reaction. Notably, the conduction band of PCN-RuCu was calculated to be -0.77 V, which is quite close to the reduction potential of CO_2/CH_4 (-0.24V). In thermodynamics, it is beneficial to the selective production of CH_4 over the PCN-RuCu sample. To obtain a deeper insight into the essence of improved selectivity of PCN-RuCu, density functional theory (DFT) calculations were performed.

3.4 DFT calculations and photocatalytic mechanism.

DFT calculations were carried out to characterize the electronic properties of PCN-RuCu. As shown in Figure 6, the analysis of density of states indicates that there is a significant bandgap in undoped PCN, while after doping of Cu and Ru, the bandgap is much narrower than undoped PCN. The projected density of states implies that the valance band maximum (VBM) is mainly contributed by the doped Ru and Cu single atoms. Especially, the pDOS of Ru is closer to the Fermi level than of Cu, suggesting that the electrons of Ru are more likely to be excited. Figure 6C shows the schematic diagram of the highest occupied molecular orbital (HOMO) of PCN-RuCu, which is mainly composed of d_{σ} orbital of Ru atom, consistent with the analysis of density of states. That is, the photogenerated electron-hole pairs will originate from the Ru single atom site of PCN-CuRu. As a result, the Ru single site will be beneficial for the proton production under reaction conditions.

Figure 6D illustrates the free-energy diagram of favorable reaction pathways for methane formation from CO_2 reduction on the Cu site and Ru site in PCN-RuCu. It is shown that the Ru site of PCN-RuCu is highly favorable for the protonation of CO_2 to CO. This is consistent with the analysis of DOS in Figure 6B, where the Fermi level is mainly comprised of Ru d states. However, the following protonation of *CO to *CHO is highly unfavorable with a high reaction energy of 1.92 eV, suggesting that CO is probably a stable adsorbed species on the Ru site under realistic conditions. Therefore, we also consider the CO_2 reduction process on the Cu site with or without a co-adsorbed CO on the Ru site. The results show that with the adsorption of CO on the Ru site, the transformation of *CO to *CHO becomes more thermodynamically favorable than Cu or Ru single atom site. As such, in PCN-RuCu, the transformation of *CO to *CHO may preferentially occur on the Cu atom sites with co-adsorbed CO on Ru site. In conclusion, the existence of Ru single atom is crucial for proton production and the Cu single atom accounts for the reduction process. The co-existence of Ru and Cu single atoms on PCN-RuCu shows great synergy to converse CO_2 to CH_4 efficiently.

Based on the above results, the possible mechanism of photocatalytic reduction of CO_2 to CH_4 over PCN-RuCu sample is presented in Figure 7. Under light illumination, the photogenerated electrons are excited from Ru sites and quickly transfer to the adjacent Cu atoms. The Cu single atom serves as an adsorption site to capture CO_2. In fact, the photocatalyst was put into $NaHCO_3$ saturated solution. Hence, CO_2 in the form of HCO_3^- is converted into *COOH, which is sequentially protonated to be *CO. Because of the synergetic effect between Ru single atom and Cu single atom, *CO can quickly experience the following consecutive hydrogenation reactions. Therefore, this feature gives CH_4 selective production of nearly 95% in the PCN-RuCu sample.

4. Conclusion

In summary, the dual Ru and Cu atoms-decorated PCN photocatalysts (PCN-RuCu) have been successfully prepared by using a preassembly-coprecipitation-pyrolysis method. The as-prepared PCN-RuCu sample displays a highly selective and efficient photocatalytic reduction of CO_2 to CH_4. Notably, the incorporation of Ru single atom significantly boosts the protonation of *CO intermediate to *CHO, which makes the rate-determining step (*CO $\rightarrow$ *CHO) over PCN-RuCu more favorable to occur. Herein, the existence of Ru single atom is crucial for proton production and the Cu single atom accounts for the reduction process. The high selectivity is attributed to the synergetic effect between Ru single atom and Cu single atom. As a result, the PCN-RuCu photocatalyst shows 95% selectivity for CH_4 production after 8 hours of visible light irradiation.

Acknowledgements

This work was supported by the Ministry of Education, Singapore, under AcRF-Tier2 (MOE2018-T2-1-017) and AcRF-Tier1 (MOE2019-T1-002-012, RG102/19). The authors also thank the support from NTU seed funding for Solar Fuels Laboratory. LH thanks for the financial support from Shenzhen Clean Energy Research Institute (CERI-KY-2019-003).

Appendix A. Supporting information

Supplementary data associated with this article can be found in the online version, at

References

[1] W. Zhang, A. R. Mohamed, W. J. Ong, Angew. Chem. Int., Ed. **2020**, 59, 22894.
[2] C. Rivera-Cárcamo, C. Scarfiello, A. B. García, Y. Tison, H. Martinez, W. Baaziz, O. Ersen, C. Le Berre, P. Serp, Adv. Mater. Interfaces **2020**, 8, 2001777.
[3] L. Wang, W. Chen, D. Zhang, Y. Du, R. Amal, S. Qiao, J. Wu, Z. Yin, Chem. Soc. Rev. **2019**, 48, 5310.
[4] K. Li, B. Peng, T. Peng, ACS Catal. **2016**, 6, 7485.
[5] Y. Xi, X. Zhang, Y. Shen, W. Dong, Z. Fan, K. Wang, S. Zhong, S. Bai, Appl. Catal. B: Environ. **2021**, 297, 120411.
[6] F. Raziq, M. Humayun, A. Ali, T. Wang, A. Khan, Q. Fu, W. Luo, H. Zeng, Z. Zheng, B. Khan, H. Shen, X. Zu, S. Li, L. Qiao, Appl. Catal. B: Environ. **2018**, 237, 1082.
[7] B. Khan, F. Raziq, M. Bilal Faheem, M. Umar Farooq, S. Hussain, F. Ali, A. Ullah, A. Mavlonov, Y. Zhao, Z. Liu, H. Tian, H. Shen, X. Zu, S. Li, H. Xiao, X. Xiang, L. Qiao, J. Hazard. Mater. **2020**, 381, 120972.
[8] F. Raziq, J. He, J. Gan, M. Humayun, M. B. Faheem, A. Iqbal, A. Hayat, S. Fazal, J. Yi, Y. Zhao, K. Dhanabalan, X. Wu, A. Mavlonov, T. Ali, F. Hassan, X. Xiang, X. Zu, H. Shen, S. Li, L. Qiao, Appl. Catal. B: Environ. **2020**, 270, 118870.
[9] F. Raziq, A. Hayat, M. Humayun, S. K. Baburao Mane, M. B. Faheem, A. Ali, Y. Zhao, S. Han, C. Cai, W. Li, D.-C. Qi, J. Yi, X. Yu, M. B. H. Breese, F. Hassan, F. Ali, A. Mavlonov, K. Dhanabalan, X. Xiang, X. Zu, S. Li, L. Qiao, Appl. Catal. B: Environ. **2020**, 270, 118867.
[10] A. Kumar, P. Raizada, A. Hosseini-Bandegharaei, V. K. Thakur, V.-H. Nguyen, P. Singh, J. Mater. Chem. A **2021**, 9, 111.
[11] S. N. Talapaneni, G. Singh, I. Y. Kim, K. AlBahily, A. H. Al-Muhtaseb, A. S. Karakoti, E. Tavakkoli, A. Vinu, Adv. Mater. **2019**, 1904635.
[12] C. Gao, S. Chen, Y. Wang, J. Wang, X. Zheng, J. Zhu, L. Song, W. Zhang, Y. Xiong, Adv. Mater. **2018**, 30, 1704624.
[13] L. Zeng, C. Xue, Nano Research **2020**, 14, 934.
[14] M. Zhao, J. Feng, W. Yang, S. Song, H. Zhang, ChemCatChem **2020**, 13, 1250.
[15] Z. Chen, S. Mitchell, E. Vorobyeva, R. K. Leary, R. Hauert, T. Furnival, Q. M. Ramasse, J. M. Thomas, P. A. Midgley, D. Dontsova, M. Antonietti, S. Pogodin, N. López, J. Pérez-Ramírez, Adv. Funct. Mater. **2017**, 27, 1605785.
[16] Z. Chen, E. Vorobyeva, S. Mitchell, E. Fako, N. López, S. M. Collins, R. K. Leary, P. A. Midgley, R. Hauert, J. Pérez-Ramírez, Natl. Sci. Rev. **2018**, 5, 642.
[17] Z. Chen, S. Mitchell, F. Krumeich, R. Hauert, S. Yakunin, M. V. Kovalenko, J. Pérez-Ramírez, ACS Sustain. Chem. Engineering **2019**, 7, 5223.
[18] Q. Wang, D. Zhang, Y. Chen, W.-F. Fu, X.-J. Lv, ACS Sustain. Chem. Engineering **2019**, 7, 6430.
[19] G. Wang, T. Zhang, W. Yu, R. Si, Y. Liu, Z. Zhao, ACS Catal. **2020**, 10, 5715.
[20] L. Zeng, C. Dai, B. Liu, C. Xue, J. Mater. Chem. A **2019**, 7, 24217.
[21] Z. Guo, Y. Xie, J. Xiao, Z. J. Zhao, Y. Wang, Z. Xu, Y. Zhang, L. Yin, H. Cao, J. Gong, J. Am. Chem. Soc. **2019**, 141, 12005.
[22] P. Zhou, X. Hou, Y. Chao, W. Yang, W. Zhang, Z. Mu, J. Lai, F. Lv, K. Yang, Y. Liu, J. Li, J. Ma, J. Luo, S. Guo, Chem. Sci. **2019**, 10, 5898.
[23] W. Liu, L. Cao, W. Cheng, Y. Cao, X. Liu, W. Zhang, X. Mou, L. Jin, X. Zheng, W. Che, Q. Liu, T. Yao, S. Wei, Angew. Chem. Int., Ed. **2017**, 56, 9312.
[24] Y. Zhou, L. Zhang, W. Wang, Nat. Commun. **2019**, 10, 506.

[25] J. Wen, X. Yang, Z. Sun, J. Yang, P. Han, Q. Liu, H. Dong, M. Gu, L. Huang, H. Wang, Green Chem. **2020**, 22, 230.
[26] P. Chen, B. Lei, X. Dong, H. Wang, J. Sheng, W. Cui, J. Li, Y. Sun, Z. Wang, F. Dong, ACS Nano **2020**, 14, 15841.
[27] S. Ji, Y. Qu, T. Wang, Y. Chen, G. Wang, X. Li, J. Dong, Q. Chen, W. Zhang, Z. Zhang, S. Liang, R. Yu, Y. Wang, D. Wang, Y. Li, Angew. Chem. Int., Ed. **2020**, 132, 2.
[28] Y. Li, B. Li, D. Zhang, L. Cheng, Q. Xiang, ACS Nano **2020**, 14, 10552.
[29] J. Wang, T. Heil, B. Zhu, C. W. Tung, J. Yu, H. M. Chen, M. Antonietti, S. Cao, ACS Nano **2020**, 14, 8584.
[30] H. Li, J. Sun, ACS Appl. Mater. Interfaces **2021**, 13, 5073.
[31] G. Wang, C. T. He, R. Huang, J. Mao, D. Wang, Y. Li, J. Am. Chem. Soc. **2020**, 142, 19339.
[32] A. Guan, Z. Chen, Y. Quan, C. Peng, Z. Wang, T.-K. Sham, C. Yang, Y. Ji, L. Qian, X. Xu, G. Zheng, ACS Energy Lett. **2020**, 5, 1044.
[33] K. Zhao, X. Nie, H. Wang, S. Chen, X. Quan, H. Yu, W. Choi, G. Zhang, B. Kim, J. G. Chen, Nat. Commun. **2020**, 11, 2455.
[34] J. Jiao, R. Lin, S. Liu, W. C. Cheong, C. Zhang, Z. Chen, Y. Pan, J. Tang, K. Wu, S. F. Hung, H. M. Chen, L. Zheng, Q. Lu, X. Yang, B. Xu, H. Xiao, J. Li, D. Wang, Q. Peng, C. Chen, Y. Li, Nat. Chem. **2019**, 11, 222.
[35] G. Kresse, J. Furthmüller, Comput. Mater. Sci. **1996**, 6, 15.
[36] G. Kresse, J. Furthmuller, Phys. Rev. B **1996**, 54, 11169.
[37] J. P. Perdew, K. Burke, M. Ernzerhof, Phys. Rev. Lett. **1996**, 77, 3865.
[38] H. J. Monkhorst, J. D. Pack, Phys. Rev. B **1976**, 13, 5188.
[39] J. VandeVondele, M. Krack, F. Mohamed, M. Parrinello, T. Chassaing, J. Hutter, Comput. Phys. Commun. **2005**, 167, 103.
[40] K. Mathew, R. Sundararaman, K. Letchworth-Weaver, T. A. Arias, R. G. Hennig, J. Chem. Phys. **2014**, 140, 084106.
[41] Q. Liu, J. Zhang, Langmuir. **2013**, 29, 3821.
[42] F. Wang, Y. Wang, Y. Li, X. Cui, Q. Zhang, Z. Xie, H. Liu, Y. Feng, W. Lv, G. Liu, Dalton Trans. **2018**, 47, 6924.
[43] T. Zhang, D. Zhang, X. Han, T. Dong, X. Guo, C. Song, R. Si, W. Liu, Y. Liu, Z. Zhao, J. Am. Chem. Soc. **2018**, 140, 16936.
[44] Y. Wang, Z. Chen, P. Han, Y. Du, Z. Gu, X. Xu, G. Zheng, ACS Catal. **2018**, 8, 7113.
[45] X. Peng, H.-X. Liu, Y. Zhang, Z.-Q. Huang, L. Yang, Y. Jiang, X. Wang, L. Zheng, C. Chang, C.-t. Au, L. Jiang, J. Li, Chem. Sci. **2021**, 12, 7125-7137.
[46] Y. Yao, S. Hu, W. Chen, Z.-Q. Huang, W. Wei, T. Yao, R. Liu, K. Zang, X. Wang, G. Wu, W. Yuan, T. Yuan, B. Zhu, W. Liu, Z. Li, D. He, Z. Xue, Y. Wang, X. Zheng, J. Dong, C.-R. Chang, Y. Chen, X. Hong, J. Luo, S. Wei, W.-X. Li, P. Strasser, Y. Wu, Y. Li, Nat. Catal. **2019**, 2, 304.
[47] F. Li, G.-F. Han, H.-J. Noh, S.-J. Kim, Y. Lu, H. Y. Jeong, Z. Fu, J.-B. Baek, Energy Environ. Sci. **2018**, 11, 2263.
[48] Y. Qu, Z. Li, W. Chen, Y. Lin, T. Yuan, Z. Yang, C. Zhao, J. Wang, C. Zhao, X. Wang, F. Zhou, Z. Zhuang, Y. Wu, Y. Li, Nat. Catal. **2018**, 1, 781.
[49] F. Zhang, J. Zhang, J. Li, X. Jin, Y. Li, M. Wu, X. Kang, T. Hu, X. Wang, W. Ren, G. Zhang, J. Mater. Chem. A **2019**, 7, 6939.
[50] S. Cao, H. Li, T. Tong, H.-C. Chen, A. Yu, J. Yu, H. M. Chen, Adv. Funct. Mater. **2018**, 28, 1802169.
[51] X.-W. Guo, S.-M. Chen, H.-J. Wang, Z.-M. Zhang, H. Lin, L. Song, T.-B. Lu, J. Mater. Chem. A **2019**, 7, 19831.
[52] R. Trofimovaite, C. M. A. Parlett, S. Kumar, L. Frattini, M. A. Isaacs, K. Wilson, L. Olivi, B. Coulson, J. Debgupta, R. E. Douthwaite, A. F. Lee, Appl. Catal. B: Environ. **2018**, 232, 501.
[53] D. Zhao, Y. Wang, C.-L. Dong, Y.-C. Huang, J. Chen, F. Xue, S. Shen, L. Guo, Nat. Energy **2021**, 6, 388.

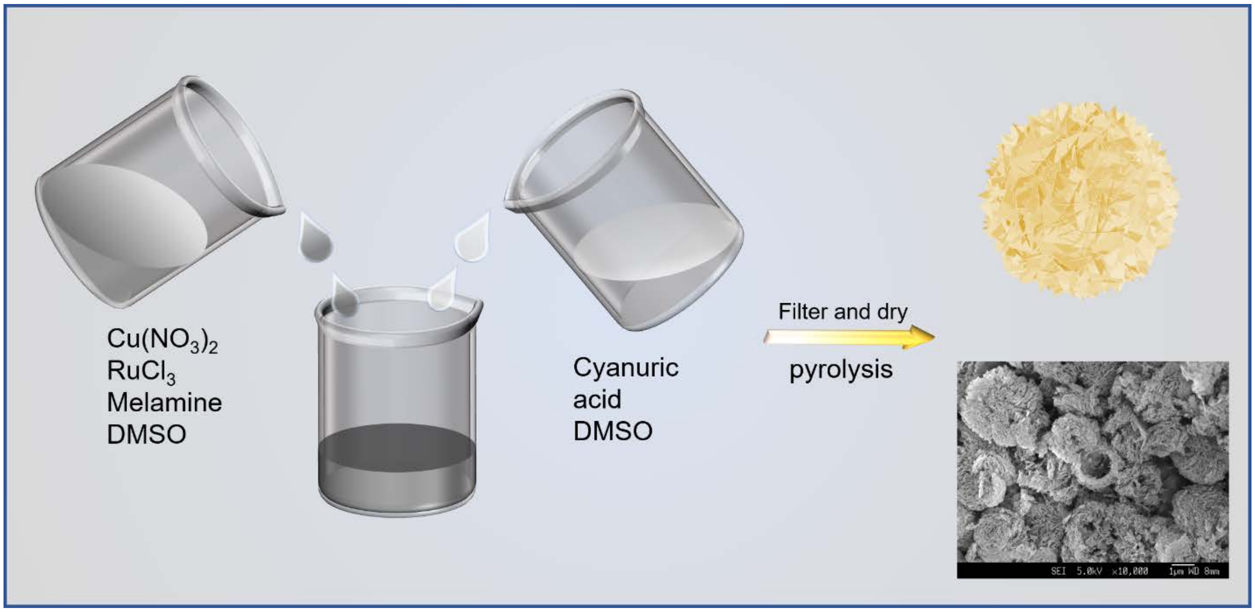

Figure 1. Schematic diagram of PCN-RuCu catalyst synthesis process

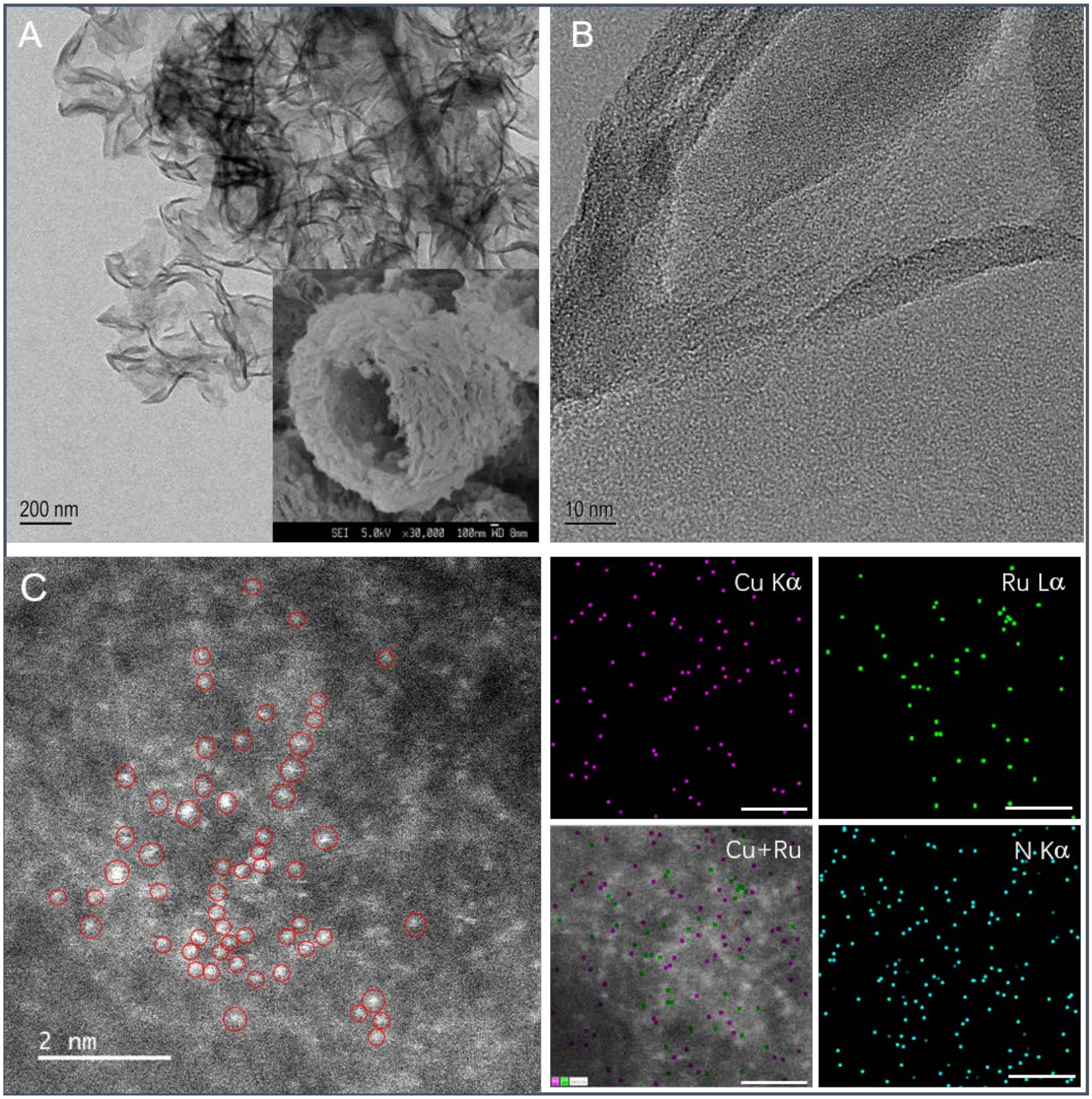

Figure 2. TEM and SEM image (A), HR-TEM image (B), aberration corrected HAADF-STEM image (C) of PCN-RuCu SAC and EDS mapping of each elements (scale bar is 2nm)

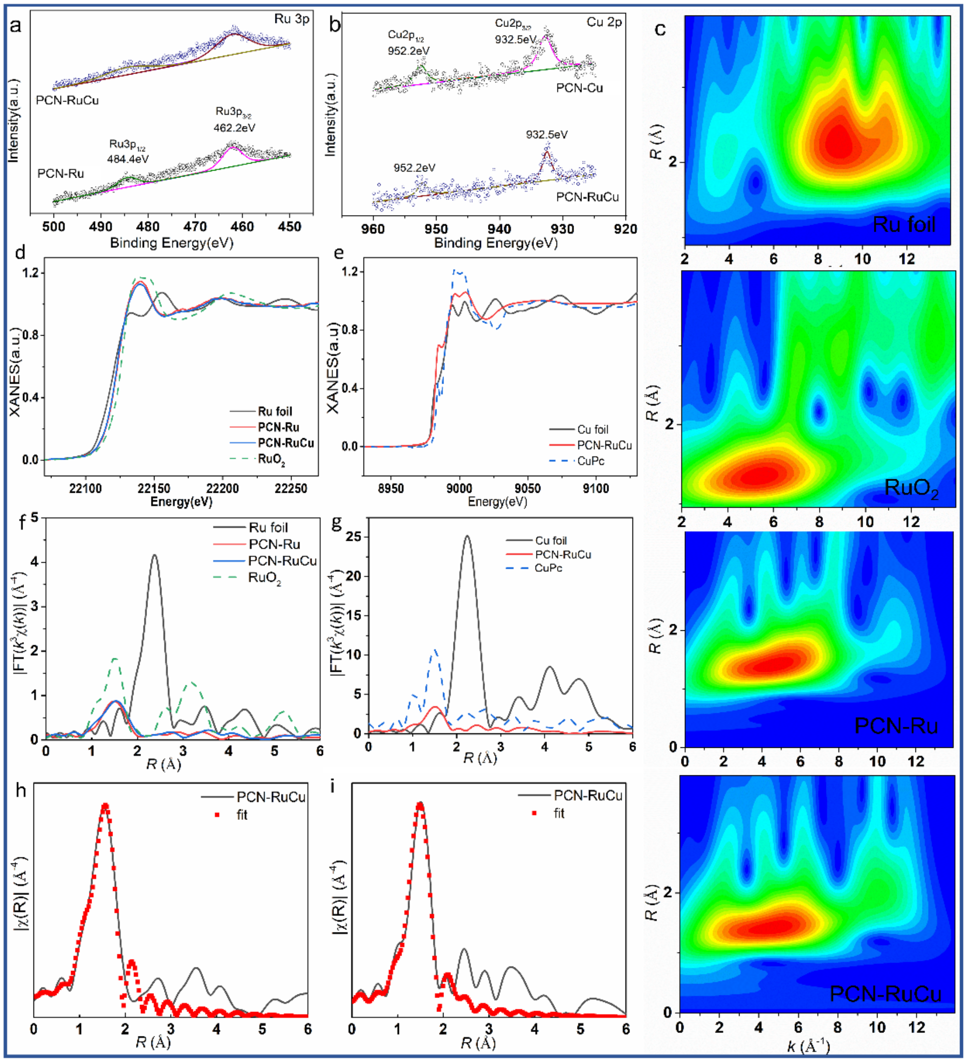

Figure 3. (a) Ru 3p XPS spectra of PCN-Ru and PCN-RuCu. (b) Cu 2p XPS spectra of PCN-Cu and PCN-RuCu. (c) Wavelet transform EXAFS plots of Ru foil, RuO_2, PCN-Ru and PCN-RuCu. (d) Normalized Ru K-edge XANES of Ru foil, PCN-Ru, PCN-RuCu and RuO_2. (e) Normalized Cu K-edge XANES of Cu foil, PCN-RuCu and CuPc(copper phthalocyanine). (f) k^3-weight Fourier transform spectra from Ru K-edge EXAFS. (g) k^3-weight Fourier transform spectra from Cu K-edge EXAFS. (h) The k^3-weight FT-EXAFS fitting curves of PCN-RuCu at Ru K-edge. (i) The k^3-weight FT-EXAFS fitting curves of PCN-RuCu at Cu K-edge.

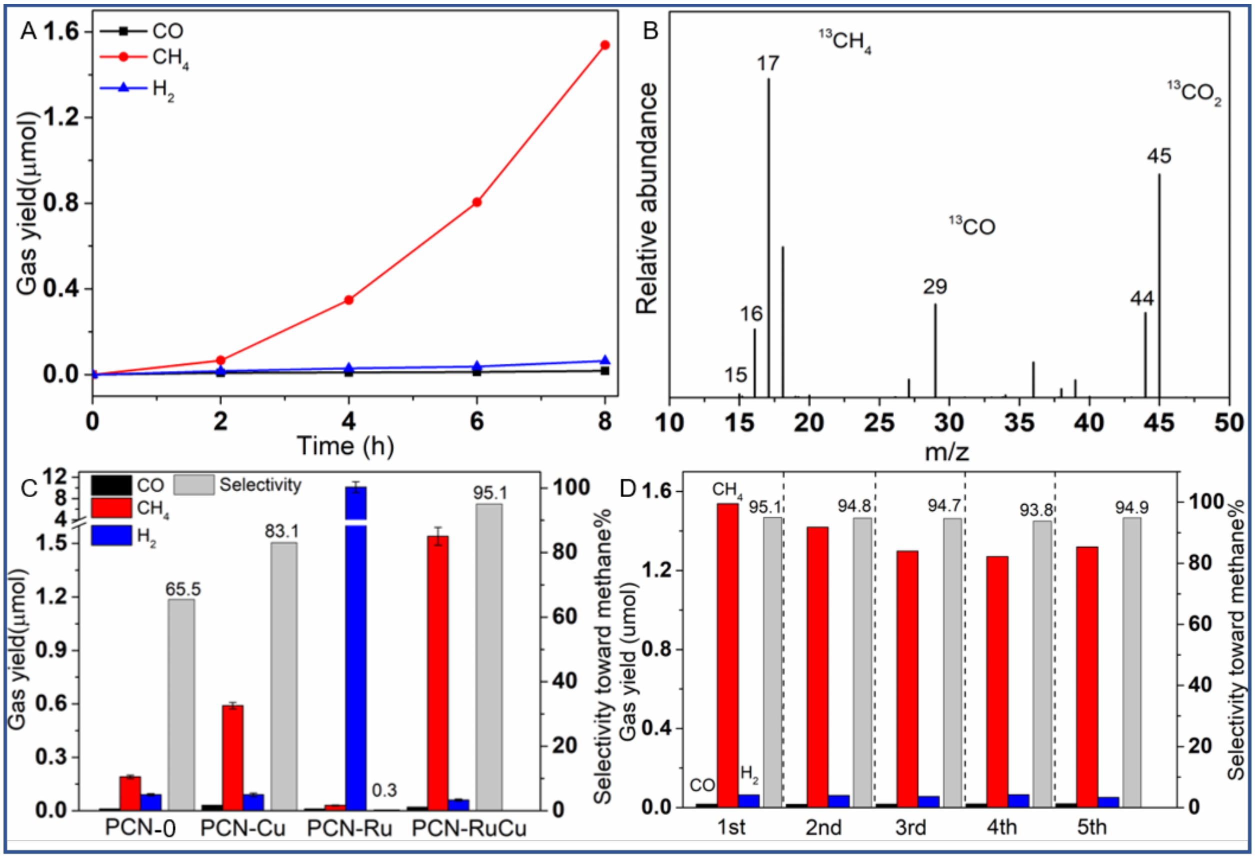

Figure 4. The evolution of all gaseous products with reaction duration over PCN-RuCu sample (A). Mass spectra of $^{13}CH_4$ (m/z=17), ^{13}CO (m/z=29) produced over PCN-RuCu sample in the photocatalytic reduction of $^{13}CO_2$ (m/z=45) after 24 hours' visible light irradiation (B). Gas yield and selectivity towards methane for PCN-Cu SAC, PCN-Ru SAC and PCN-RuCu SAC after 8 hrs visible light irradiation (C). The cycle test for PCN-RuCu sample (D).

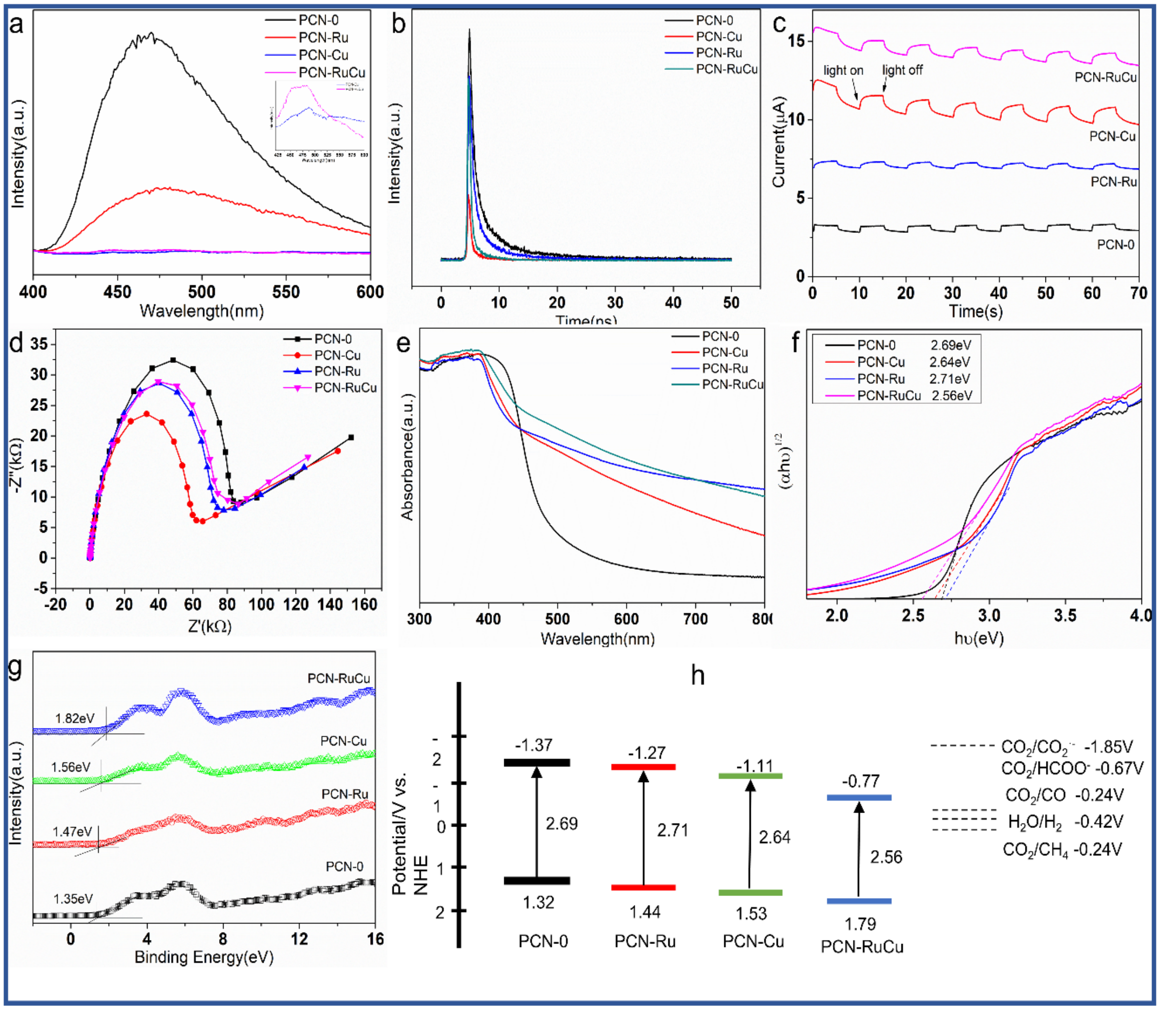

Figure 5. (a) Photoluminescence spectra for PCN-0, PCN-Ru, PCN-Cu and PCN-RuCu, the insert is the magnified image of PL spectra for PCN-Cu and PCN-RuCu. (b) Time-resolved transient PL decay spectra. (c) Transient photocurrent curves. (d) EIS Nyquist plots. (e) UV-vis DRS spectra. (f) Corresponding Tauc plots for all samples calculated by using Kubelka-Munk formula. (g) VB XPS spectra. (h) Band structure alignments for all samples and redox potential of partial reactions.

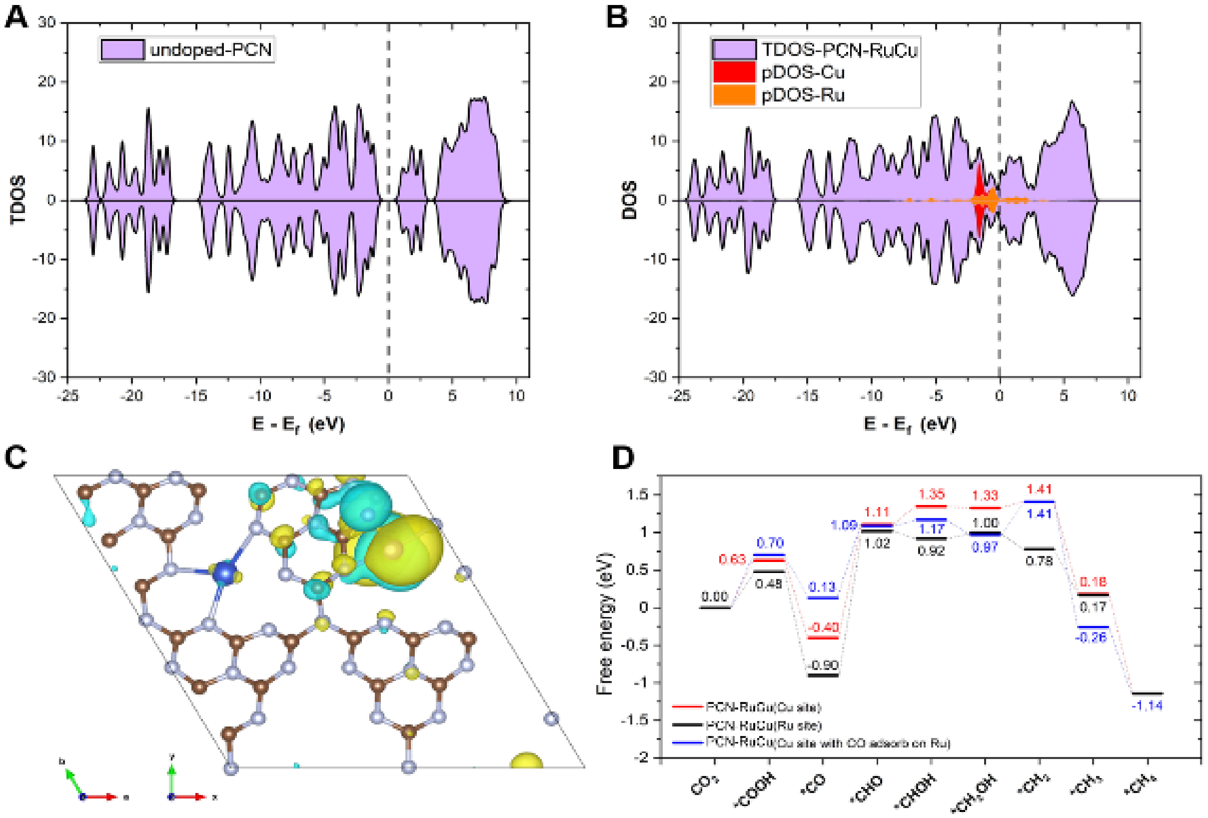

Figure 6. Calculated electronic properties and free-energy diagram for CO_2 reduction to CH_4 on PCN-RuCu. (A) TDOS of undoped PCN (B) TDOS of PCN-RuCu and pDOS of Cu (red) and Ru (Orange) on PCN-RuCu. (C) Schematic diagram of HOMO of PCN-RuCu. (D) Calculated free-energy diagram for CO_2 reduction to CH_4 on Cu and Ru site of PCN-RuCu. Free-energy diagram of Cu site with CO adsorbs on Ru site of PCN-RuCu is also calculated. The Ru, Cu, C, N and O atoms are given in white, purple, brown, silver and red, respectively.

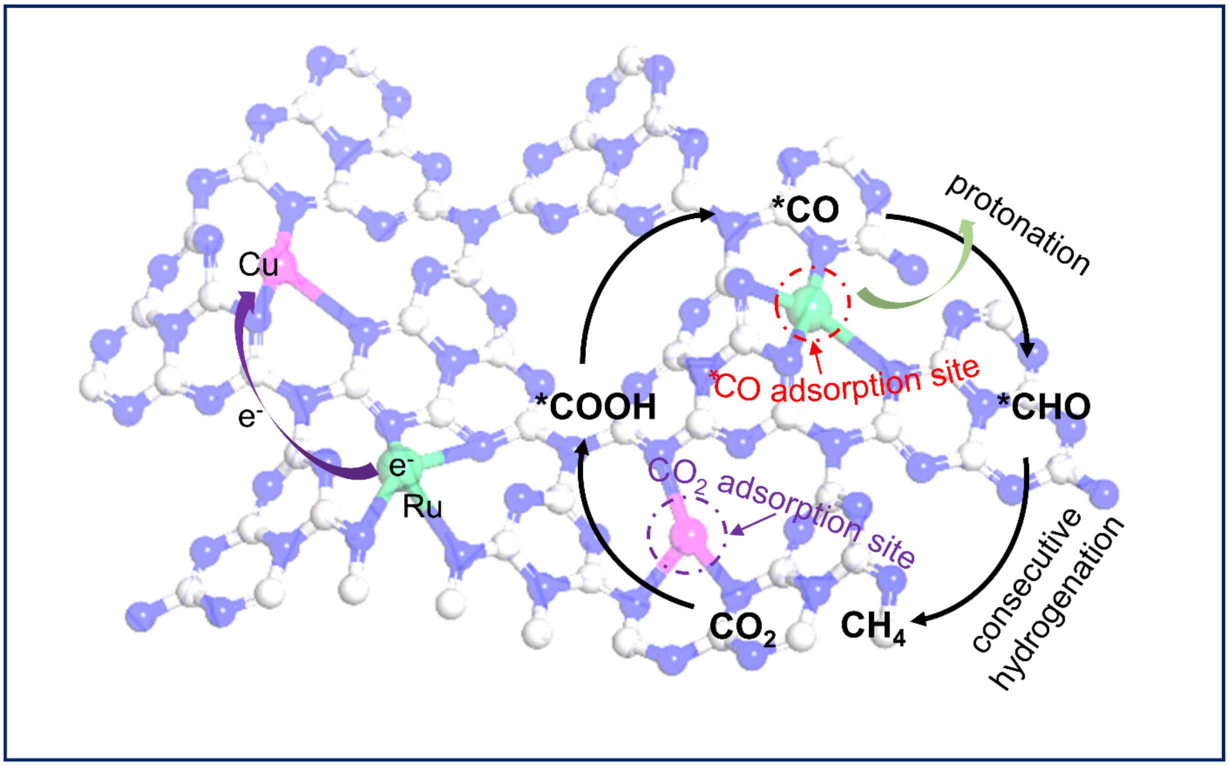

Figure 7. Schematic of the possible photocatalytic mechanism of PCN-RuCu sample for photocatalytic CO_2 reduction under light illumination. The "*" represents the adsorption site on substrate. Nitrogen, carbon, ruthenium and copper atoms are shown in blue, grey, green and pale red, respectively.